Hydrogen-reduced bismuth oxyiodide nanoflake arrays with plasmonic enhancements for efficient photoelectrochemical water reduction

Jiayong Gan, Bharath Bangalore Rajeeva, Zilong Wu, Daniel Penley, Yuebing Zheng*

Department of Mechanical Engineering, Materials Science and Engineering Program, and Texas Materials Institute, The University of Texas at Austin, Austin, Texas 78712, United States

A B S T R A C T

Bismuth oxyiodide has attracted strong interest as a nano-engineered material for high-performance electrodes in photoelectrochemical (PEC) cells. Herein, we demonstrate the visible-light-sensitive PEC photocathodes based on nano-engineered bismuth oxyiodide (BiOI). The photocathodes are comprised of plasmonic Au nanoparticles (NPs) on hydrogen-reduced BiOI (H-BiOI) nanoflake arrays. The BiOI-based photocathodes exhibit an AM 1.5 photocurrent of $3.6 \pm 0.1\,\mathrm{mA/cm^2}$ at $0\,\mathrm{V}$ vs reversible hydrogen electrode. We attribute the enhanced photoreduction performance of our photocathodes to three factors that increase the formation and separation rates of electron-hole pairs for photocatalysis. Firstly, the small thickness of the nanoflakes facilitates the diffusion of minority carriers to the surfaces before their recombination. Secondly, the hydrogenation-induced oxygen vacancies in H-BiOI lead to increased acceptor density. Lastly, plasmonic effects in Au NPs enhance the light absorption, hot-carrier injection, and resonant energy transfer in the composite electrodes. Our experiments are coupled to optical simulations. This work demonstrates the tremendous potential of coupling plasmonic effects with nano-engineering to innovate visible-light-sensitive photocathodes for the realization of efficient PEC cells.

© 2016 Elsevier Ltd. All rights reserved.

1. Introduction

Photoelectrochemical (PEC) cells split water into hydrogen and oxygen using sunlight. The production of chemical fuels by solar energy conversion is a sustainable solution to the present energy problem [1–3]. There are enormous research efforts in exploring new semiconductor materials as efficient photoelectrodes to enhance PEC efficiency, which depends on light absorption, charge separation, transportation, and recombination processes at the electrodes [4–6]. Since wide-bandgap semiconductors such as TiO_2, ZnO, SnO_2, and WO_3 have a limited ability to absorb visible light [7–10], narrow-bandgap semiconductors have been highly pursued.

Due to its small bandgap of 1.6–1.9 eV and unique structures, bismuth oxyiodide (BiOI) is one of the most attractive visible-light-driven photocatalysts [11–14]. BiOI has an open, layered crystal structure consisted of $[Bi_2O_2]^{2+}$ layers sandwiched between two slabs of halogen ions [15]. The interleaved layer structure between positive $[Bi_2O_2]^{2+}$ slabs and negative iodide slabs builds spontaneous internal static electric fields, which facilitate the effective charge separation and transfer [11,16,17]. The dispersive band characteristics of BiOI could also contribute to the high photocatalytic activity since multiple pathways are allowed for the excitation of electrons. However, BiOI photoelectrodes have exhibited low photocatalytic efficiency due to the limited conductivity and high recombination rate of photogenerated charge carriers. Herein, we demonstrate high-performance BiOI-based photocathodes by synergizing hydrogenation, nanostructuring, and plasmonic effects of Au nanoparticles (NPs).

The field of plasmonics has expanded rapidly for many applications such as solar water splitting and solar cells due to the unique capability of plasmonic nanostructures in managing light at the nanoscale [18–21]. Other applications include near-field optics [22,23], surface-enhanced spectroscopy [24,25], plasmon waveguides [26], biomedical imaging [27], metamaterials [28], and medicine [29,30]. The advantages of plasmonic nanostructures in solar-energy harvesting applications are multifold [31,32]. Plasmonic nanostructures have been found to enhance the solar-energy conversion efficiency in the PEC cells via multiple mechanisms: (i) plasmon-induced hot electron injection into the

* Corresponding author.
  E-mail address: zheng@austin.utexas.edu (Y. Zheng).

conduction band of the semiconductors (n-type) [33], (ii) near-field electromagnetic concentration for enhanced light absorption by the semiconductors [34], (iii) plasmon resonance energy transfer (PRET) from plasmonic nanostructures to the adjacent semiconductors, (iv) plasmonic heating, and (v) plasmon-enhanced light scattering [35]. With a proper design of the composite photoelectrodes consisted of plasmonic and semiconductor nanostructures, one can fully exploit the plasmonic effects to enhance the energy efficiency of PEC cells. Meanwhile, controlling oxygen vacancies in semiconductor electrodes has proven to be effective in enhancing PEC performance [36–38].

Herein, we show that hydrogen-reduced BiOI (H-BiOI) nanoflakes arrays (NFAs) incorporating plasmonic Au NPs work as photocathodes for efficient PEC water reduction, which exhibits both improved photocurrent response and solar energy conversion efficiency. We reveal that oxygen vacancies in H-BiOI introduce shallow acceptor levels, which facilitate hole transfer at the interface between BiOI and substrates as well as the interface between BiOI and electrolytes. Furthermore, the plasmonic effects in Au NPs enhance light absorption, hot-carrier injection, and resonant energy transfer in the photocathodes. With advantages of improved electrical conductivity, high surface areas of NFAs, and plasmonic effects, our Au@H-BiOI photocathodes exhibit an AM 1.5G photocurrent density of 3.6 ± 0.1 mA/cm^2 at 0 V versus reversible hydrogen electrode (RHE) with over 80% Faradaic efficiency, which is higher than other BiOI electrodes previously reported [17,39]. The maximum photoconversion efficiency can reach 0.55% with a photocurrent of 0.95 mA/cm^2. To the best of our knowledge, this is the first demonstration of combining plasmonic effects with oxygen vacancies in p-type BiOI photocathodes to promote the PEC performance, which opens up new opportunities for both the fundamental study of plasmonic effects in p-type semiconductors and the design of robust, efficient tandem or hybrid high-performance photocathodes for PEC cells.

2. Materials and Methods

2.1. Synthesis of BiOI NFAs

All the reagents were of analytical grade and used without any further purification. Deionized (DI) water was used in all experiments. BiOI NFA films were synthesized on fluorine-doped tin oxide (FTO) glass substrates using an electrodeposition method reported previously [40]. Briefly, 50 mL of 0.8 M Bi(NO$_3$)$_3$ and 8 M KI (pH = 1.7) were added to 20 mL of 0.23 M p-benzoquinone absolute ethanol solution. Pt wire and saturated Ag/AgCl were used as the counter electrode and reference electrode in all the electrochemical experiments. The cathodic deposition was carried out potentiostatically at −0.14 V for 3 mins. The samples were rinsed with DI water and dried at room temperature.

2.2. Hydrogen Treatment for Preparation of H-BiOI

Hydrogen treatment was carried out in an MTI tube furnace. The as-deposited BiOI thin films were annealed in a pure hydrogen atmosphere (99.9%, 1 bar, 50 sccm gas flow) for 20 mins at variable temperatures.

2.3. Deposition of Au NPs on BiOI/H-BiOI NFAs

Au NPs were deposited on BiOI NFAs using an AC sputtering system (Denton Vacuum Desk II Gold sputter). The coverage of Au NPs was controlled by sputtering time at a constant current of 50 mA.

2.4. Structural and compositional characterizations

The structures and compositions of the samples were characterized with scanning electron microscopy (SEM) (FEI Quanta 650), transmission electron microscopy (TEM) (200 kV, JEM2010-HR), and X-ray diffractometer (XRD) (Rikagu MiniFlex 600). Total transmittance and diffuse reflectance spectra were measured with a Cary 500 UV-Vis-NIR spectrophotometer attached to a Labsphere DRA-CA-5500 integrating sphere. A bare FTO substrate was employed as a baseline standard, and corrected values of transmittance (T) were used to calculate the absorbance (A) using:

$$A = -\log_{10}(T) \tag{1}$$

X-ray photoelectron spectroscopy (XPS) measurements were performed on a Kratos AXIS Ultra DLD spectrometer with a monochromated Al Kα X-ray source (hν = 1486.5 eV). CasaXPS (Version 2.3.15) software was used to analyze the XPS spectra. The adventitious carbon 1 s peak was used as a reference with a binding energy (B.E.) of 285 eV.

2.5. PEC measurements and analyses

PEC measurements were conducted in a 3-neck glass electrode cell with the sample being measured as the working electrode. The illumination source was a 150 W Xe arc lamp (Newport, 6255) directed at the quartz PEC cell (100 mW/cm^2). All the electrochemical measurements were performed on a CHI 660E electrochemical workstation at room temperature. The electrolyte used was 0.5 M Na$_2$SO$_4$ aqueous solution. The gas evolution was conducted at the same condition with a bias of +0.2 V vs RHE. The measurements were performed in three cycles for each photocathode. Between each cycle, the solution was renewed and the test system was reset to zero.

The incident-photon-to-current conversion efficiency (IPCE) was calculated from chronoamperometry measurements using a Newport Oriel Cornerstone 130 1/8 m monochromator (Photon Technology International). The monochromator slit size was set to 0.75 mm × 2 mm, and the light power was measured with a silicon photodetector (Newport, 818-UV, Newport). The IPCE values were calculated using the following equation:

$$IPCE(\lambda) = \frac{1240 J(\lambda)}{\lambda \times P(\lambda)} \times 100\% \tag{2}$$

where λ is the wavelength (nm), $J(\lambda)$ is the photocurrent density (mA/cm^2), and $P(\lambda)$ is the incident-power density of the monochromated light (mW/cm^2). The photo-conversion efficiencies (η) of the as prepared photocathodes were calculated from the experimental J–V curves by assuming 100% Faradaic efficiency according to the following equation:

$$\eta(\lambda) = \frac{J_{PMax} \times V_{PMax}}{P_{in}} \times 100\% \tag{3}$$

where J_{Pmax} and V_{Pmax} are the current density (mW/cm^2) and photovoltage (V vs RHE) at the maximum power point and P_{in} (mW/cm^2) is the incoming light flux (100 mW/cm^2). Mott-Schottky plots were generated from capacitance obtained from the electrochemical impedance spectroscopy (EIS) measurement at each potential with a frequency of 10 kHz.

2.6. Numerical simulations

The numerical simulations on plasmonic properties of NPs were performed using FDTD Solutions (Lumerical), a commercial FDTD Maxwell Equation solver. Based on experimental measurements, a

spherical Au NP (diameter = 20 nm) on the surface of BiOI nanoplate is used as a model. Linearly polarized light is illuminated vertically onto the substrate. The reflected light and electromagnetic field were collected with a two-dimensional (2D) frequency-domain power detector and electric-field detector, respectively.

3. Results and Discussions

We comparatively studied a series of nanostructured Au@H-BiOI electrodes with variable coverage of Au NPs to understand the roles of surface plasmons and oxygen vacancies in PEC water reduction. Fig. 1 summarizes the structural and compositional properties of a representative Au@H-BiOI electrode where the sputtering time for Au NPs is 8 secs. The SEM images in Figs. 1a–c show that the H-BiOI NFAs with a thickness of ~20 nm are randomly oriented with variable gaps among them, leading to high surface areas for enhanced chemical reactions. The network of the ultra-thin H-BiOI nanoflakes is expected to have high electron-hole separation efficiency [41,42], thus allowing the generated minority carriers to diffuse to the surfaces before they recombine. The network's high surface area morphology exposes sufficient active sites to the solution, facilitating the chemical process. The plasmon-enhanced electromagnetic fields localized at the interfaces of Au NPs and BiOI (H-BiOI) can penetrate into the majority of the ultra-thin nanoflakes. The TEM image in Fig. 1d shows the formation of the Au NPs (with a mean diameter of 20 nm) on the BiOI NFAs. In Fig. 1e, the high-resolution TEM (HRTEM) image of an Au NP reveals its crystal structure. The lattice fringe spacing of 0.235 nm matches well with the Au(111) plane of face-centered cubic (FCC) structure. The XRD spectra in Fig. 1f also confirms the tetragonal structure of BiOI (JCPDS #:10-0445) and the FCC Au (JCPDS #:2-1095), indicating the crystalline phases of Au@H-BiOI.

We measured the optical absorption of BiOI, H-BiOI, Au@BiOI, and Au@H-BiOI on FTO substrates using diffused reflectance UV–vis spectroscopy. The measured transflectance (transmittance + reflectance) values of all the films and a reference FTO substrate were used to calculate absorbance values for each BiOI film. As shown in Fig. 2a, a noticeable shoulder starts at a wavelength of 640 nm in the pristine BiOI spectrum, which corresponds to the electronic band gap of the pristine BiOI (1.7–1.8 eV) [37]. For the Au@BiOI (sputtering time: 8 secs), an additional absorption centered at 568 nm appears due to the excitation of the localized surface plasmon resonances (LSPRs) of Au NPs. LSPRs can be easily tuned to overlap with the semiconductor absorption wavelengths to enhance physical and chemical properties. Precise tuning can be accomplished because the wavelength of plasmon resonance relies on the size, shape, and distribution of Au NPs which can be controlled [43]. When the sputtering time was increased to 10 secs, the LSPR peak made a redshift of 7 nm due to the increased size of the NPs and the variation of inter-particle distance. Compared with BiOI, H-BiOI has the enhanced visible-light absorption at wavelengths longer than 640 nm, which is attributed to electronic transitions between defect states and band-edge states in the H-BiOI [44]. This spectra change suggests possible modification in crystal structure of the film during hydrogen treatment. Due to the combined effects of LSPRs and hydrogenation [45], the Au@H-BiOI has a significant improvement in visible-light absorption, which can benefit the PEC performance.

We applied chopped-light linear sweep voltammetry (LSV) to characterize the pristine BiOI and H-BiOI photoelectrodes to gain insight into the effects of hydrogenation on the PEC performance. As shown in Fig. S1 in Supporting Information, the photocurrent density of pristine BiOI is 0.3 mA/cm^2 at 0 V vs RHE, which is much lower than that of H-BiOI. The photocurrent density for H-BiOI at 0 V vs RHE gradually increases and drastically decreases upon the increase in the annealing temperature for hydrogenation. The decreased photocurrent density at the higher temperature can be
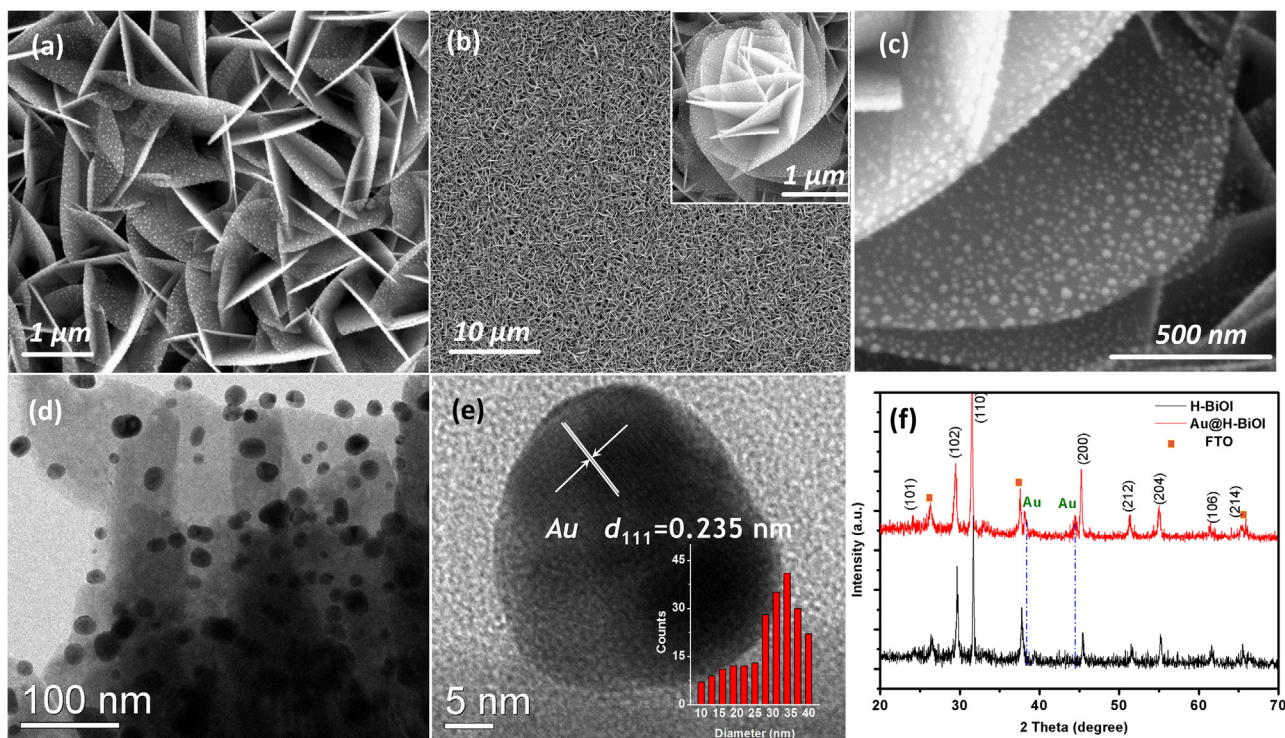
Fig. 1. SEM images of Au@H-BiOI with the different magnifications: (a) intermediate, (b) low (Inset shows the "flower" nanoarchitecture), and (c) high. TEM images of Au@H-BiOI with (d) low resolution and (e) high resolution (Inset is the size distribution of NPs). (f) XRD spectra for pristine H-BiOI and Au@H-BiOI.
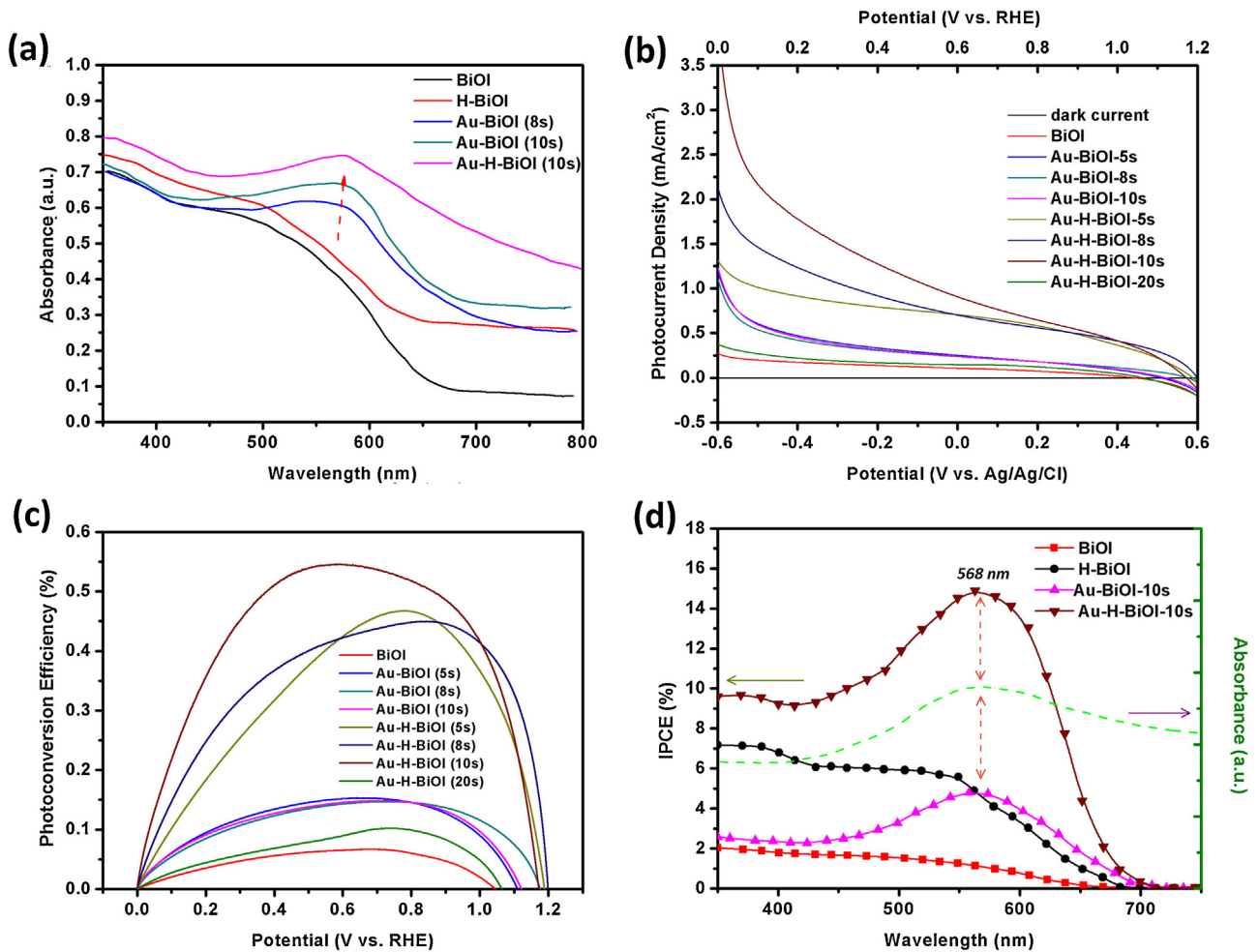
Fig. 2. (a) Optical absorption spectra of pristine BiOI, H-BiOI, Au@BiOI with sputtering time of 8 secs and 10 secs, and Au@H-BiOI with sputtering time of 10 secs. (b) Linear-sweep voltammograms for pristine BiOI, Au@BiOI, and Au@H-BiOI with different sputtering times. The measurements were carried out in a 0.2 M aqueous Na_2SO_4 with a pH of 7 under a solar simulator (AM 1.5, 100 mW/cm^2). The scan rate is 20 mV/s. The dark scan is also included. (c) Calculated solar-energy conversion efficiencies for the different photoelectrodes based on a three-electrode system. (d) IPCE spectra of pristine BiOI, H-BiOI, Au@BiOI, and Au@H-BiOI photoelectrodes. The sputtering time of Au is 10 secs. All the measurements were carried out at an applied potential of 0.1 V vs RHE. The absorbance spectrum of Au NPs is also included.

attributed to either the degradation of FTO substrates or the occurrence of excess amount of defects such as Bi and O vacancies that could possibly introduce trap states into the band gap of BiOI [45,46].

A typical LSV was applied to evaluate the effects of Au NPs and oxygen vacancies on the photocurrent of the electrodes, as shown in Fig. 2b. The dark scan led to negligible current. Under light illumination, Au@BiOI yielded an enhanced cathodic photocurrent, which reached 1.25 mA/cm^2 at 0 V vs RHE. The photocurrent densities in Au@BiOI with sputtering time of 5-10 secs double that of pristine BiOI at 0.6~0.1 V vs RHE. This suggests that decoration by Au NPs promoted the harvesting of solar light via plasmon-induced enhancement.

A larger photocurrent enhancement was observed for Au@H-BiOI. The Au@H-BiOI (with sputtering time of 10 secs) yielded a photocurrent of 3.55 mA/cm^2 at 0 V vs RHE. That is almost 18 times that of pristine BiOI (0.2 mA/cm^2). The improved photocurrent indicates the synergistic effects of plasmonic enhancements and hydrogenation in Au@H-BiOI. However, the photocurrent of Au@H-BiOI decreased when the sputtering time was further increased to 20 secs. The decreased photocurrent could be attributed to the enhanced blocking and charge-trapping effects by Au NPs with the increased size and density [47].

We calculated the photoconversion efficiencies η for BiOI, H-BiOI, and Au@H-BiOI photocathodes based on Eq. (3) [48]. Fig. 2c shows the photoconversion efficiencies as a function of applied bias potentials. The dependence of photoconversion efficiency on the Au NPs and hydrogenation is similar to that of photocurrent. The Au@H-BiOI with the sputtering time of 10 secs achieved the highest conversion efficiency of 0.55% at 0.59 V vs RHE.

To further investigate the effects of hydrogenation, we conducted the electrochemical impedance spectroscopy (EIS) on BiOI and H-BiOI at a frequency of 10 kHz. Capacitances (C) were derived from the EIS measurements as a function of potential (V), leading to Mott-Schottky plots as shown in Fig. 3. The negative slopes on both plots indicate the p-type semiconductor behaviors of both films. The plots were developed based on a planar electrode model rather than the actual nanostructured electrodes, which accounts for their deviation from a linear profile. The slopes in a linear regime of −0.4 to 0.2 V vs Ag/AgCl are used to estimate the acceptor density according to this equation:

$$N_a = (2/e_0\varepsilon\varepsilon_0)/[d(1/C^2)/dV] \qquad (4)$$

where N_a is the acceptor density, e_0 is the electron charge, ε is the dielectric constant of BiOI, ε_0 is the permittivity of vacuum, and V is the applied bias at the electrode. The acceptor densities of BiOI and H-BiOI were estimated to be 1.4×10^{16} cm^{-3} and 6.5×10^{17} cm^{-3},
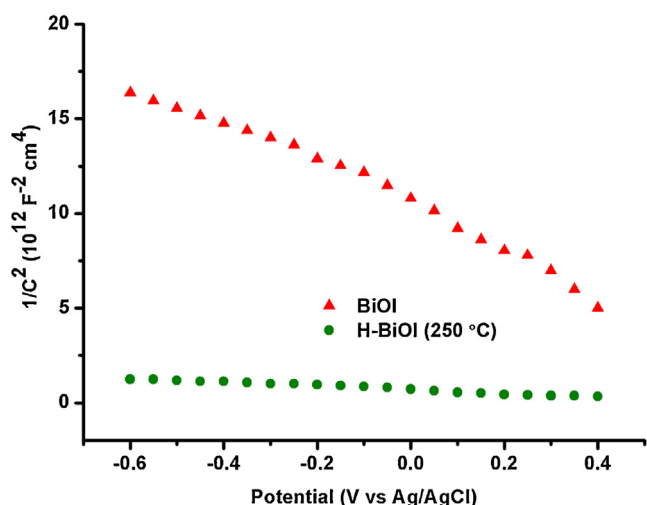
Fig. 3. Mott-Schottky plots for BiOI and H-BiOI (hydrogenation at 250 °C) based on EIS measurements in a 0.2 M phosphate buffer (pH = 7) and dark with a frequency of 10 kHz.

respectively. The increased density in H-BiOI is expected to improve the PEC performance by enhancing the carrier transfer at the interface of BiOI and FTO substrate and suppressing the bulk carrier recommendation.

To gain further insight into the physical mechanisms causing the enhanced photocurrent density by the LSPRs and hydrogenation, we measured their photoactivity as a function of the wavelength of incident light. Fig. 2d shows the IPCE data for the pristine BiOI, H-BiOI, Au@BiOI, and Au@H-BiOI, which were measured (at 0.1 V vs RHE) under the same conditions. The absorbance of Au NPs is also included for a comparison. The IPCE spectrum of pristine BiOI has a low conversion efficiency with wavelengths from 350 to 550 nm and becomes negligible (<1%) with wavelengths longer than 630 nm (corresponding to the optical absorption edge of BiOI). The H-BiOI has a larger IPCE enhancement towards the short-wavelength regime. The EIS measurements reveal that the H-BiOI NFAs exhibited a substantially smaller Mott-Schottky slope compared to pristine BiOI electrodes, indicating that either the acceptor density of BiOI NFAs was increased after the hydrogenation or there was a change in the dielectric constant of the films [49]. We believe that the hydrogenation-induced oxygen vacancies (Fig. S2) act as shallow acceptors, introducing acceptor levels in the band gap, thus altering the electronic states [50]. The hole transport in BiOI is facilitated and the Fermi level of BiOI is shifted toward its valence band [51–53]. As a result, the oxygen vacancies can facilitate carrier separation at the interface of the semiconductor and the electrolyte by increasing the band bending. Therefore, the bulk recombination was suppressed.

Au@BiOI samples exhibit different IPCE enhancement behaviors from H-BiOI. By comparing the BiOI and Au@BiOI curves in Fig. 2d, we can see that the addition of Au NPs enhances the photocurrent with the wavelengths from 550 to 580 nm. This matches the wavelength range of the LSPRs of the NPs and thus reveals the plasmonic effects on the enhancement. By combining the plasmonic effects of Au NPs and the hydrogenation, we can achieve the largest enhancement of IPCE in Au@H-BiOI. To understand the physical mechanisms behind the photocurrent enhancement, we analyzed the various plasmonic effects. Light scattering and direct plasmonic heat generation effects can be excluded since the small Au NPs (~20 nm) in our samples have the minimal scattering cross section [33] and the plasmon-induced thermal energy is lower than the energy required for the splitting

of a water molecule (1.23 eV) [34]. The overlap between the optical absorption spectra of BiOI, H-BiOI, and those of Au NPs indicates that both PRET and the plasmon-enhanced light absorption by BiOI and H-BiOI can occur in the composites [54]. The latter is due to the concentrated and enhanced electromagnetic fields at the nano-flakes by the LSPRs in the Au NPs. Other possible contributors to the enhanced photocurrent could be the plasmon-induced hot-carrier injection from Au NPs to BiOI, H-BiOI, and/or the Au catalysis. The hot-carrier injection is driven by the non-radiative decay of the LSPRs in Au NPs [55].

We simulated the near-field distributions at a single Au NP on a single BiOI nanoflake upon excitation of the LSPRs using the finite-difference time-domain (FDTD) method. Fig. 4 shows the electric field distribution for the hybrid electrodes. The electromagnetic response of these films is dominated by local "hot spots" that can be seen at the edge of the Au NP. The plasmon-enhanced electrical fields at the Au NP penetrate into the BiOI nanoflake with the strongest enhancements at the Au-BiOI interface. This process results in the rapid formation of electron-hole pairs near the surface of Au NP and BiOI. Furthermore, the photon absorption rate (and hence electron-hole pair generation rate) is much higher than that of the pristine BiOI. The penetration length of the enhanced fields into the BiOI is ~20 nm. Therefore, the plasmonic NPs can effectively couple and focus light from far field into near field at the BiOI with the intensity enhancements. The near-field amplitudes lead to the significantly improved light absorption by the semiconductor at the optical energy larger than the bandgap and the resultant increased rate of formation of electron-hole pairs at the interface. Due to the small thickness of BiOI and the influence of the surface potential, the electron-hole pairs are readily separated and the distance to migrate to the BiOI surfaces, where the water-splitting reactions occur, is reduced. With the enhancements in the electron-hole pair generation, separation, and transport, the plasmonic NPs on the ultra-thin BiOI exhibit the improved PEC performance.

Fig. 5 proposes multiple performance-enhancement mechanisms for the Au@H-BiOI photocathodes, which occur due to the effects of hydrogenation of BiOI and LSPRs of Au NPs. Firstly, hydrogen treatment creates oxygen vacancies in the BiOI NFAs, which introduces shallow acceptor levels in the band gap of BiOI [50]. Ionization of these levels activates the conduction process. Upon the light illumination, electrons can transit from either the valence band to the oxygen vacancy energy levels or from the oxygen vacancy energy levels to the conduction band [43]. Meanwhile, the increase of oxygen vacancies enhances acceptor density in BiOI NFAs, which improves the "hole" transport [56,57]
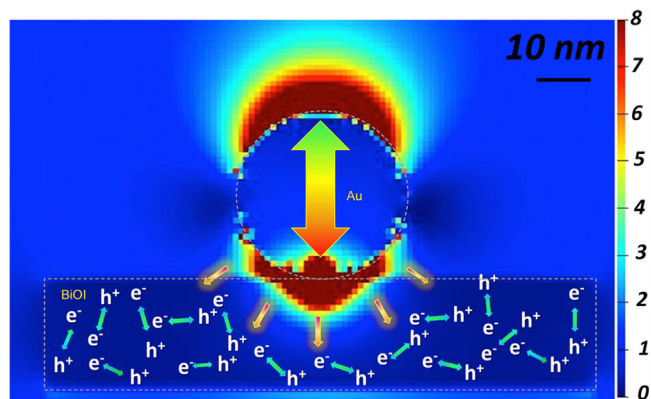
Fig. 4. A cross-sectional view of FDTD-simulated near-field electromagnetic distributions at the interface of an Au NP and a BiOI nanoflake. The dashed line indicates the outline of the nanoflake and Au NP.
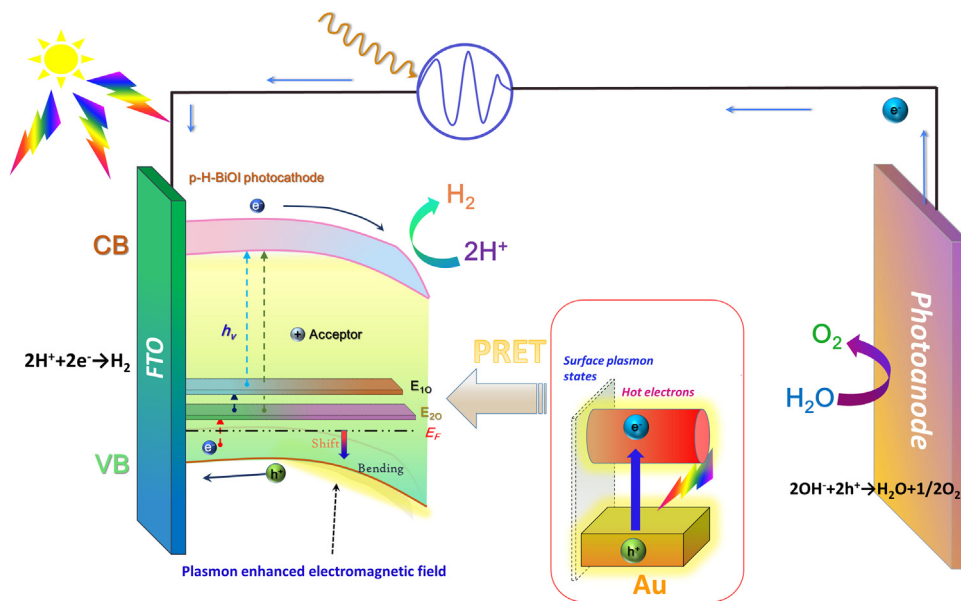
Fig. 5. Schematic illustration of the roles of surface plasmons and oxygen vacancies in the enhanced solar water splitting of the Au@H-BIOI photocathode.

both within the H-BiOI nanoflakes and at the BiOI-FTO interfaces. In addition, the Fermi level of BiOI is shifted towards its valence band due to the increased shallow acceptors, which facilitates the electron-hole separation at the BiOI-electrolyte interface by increasing the degree of band bending at the BiOI surface [53].

Further, upon excitation of the LSPRs, the Au NPs on H-BiOI can act as nanoantennas to localize the optical energy at the nanoscale around the NPs. When the optical absorption of H-BiOI has an overlap with the LSPRs of the Au NPs, the near-field electromagnetic localization and enhancements improve the light absorption by H-BiOI and facilitate the generation of electron-hole pairs. Due to the spatially inhomogeneous electromagnetic field distributions (strongest close to plasmonic Au), the highest concentration of the photoexcited electron-hole pairs occurs at the NP-H-BiOI interfaces. Moreover, the surface potential promotes the separation of electron-hole pairs and shortens their distance to travel to the H-BiOI surfaces.

In addition, the non-irradiative decay of the LSPRs on Au NPs generates hot electron carriers. The hot electrons are injected to the photocathode, trapped within the holes in H-BiOI. This may result in more efficient electron hole separation of H-BiOI. An increased amount of photoelectrons produced react with photons and in turn create better photocurrent and water reduction activity. Meanwhile, some of the hot electrons may interact with protons in the water to generate hydrogen, which has been demonstrated by Lee et al. [58,59]. Lastly, there is PRET that contributes to the carrier generation in H-BiOI.

We performed the water-splitting experiments on the PEC cells with the different types of photocathodes. Fig. 6 shows the hydrogen evolution tests at 0.2 V vs RHE. Under irradiation by AM 1.5 illumination, 29.0 ± 0.10, 7.19 ± 0.11, and 2.56 ± 0.12 µmol/h·cm^2 of H$_2$ molecules are generated by the Au@H-BiOI, Au@BiOI, and BiOI photocathodes, respectively. The theoretical amounts of the H$_2$ evolution are calculated from the corresponding photocurrent by assuming 100% Faradaic efficiency as 34.14, 9.33, and 3.15 µmol/h·cm^2, respectively. Hence, the actual faradaic efficiencies for all the electrodes are higher than 80%. BiOI is stable in neutral solutions even at a bias, leading to high Faraday efficiencies for all the samples. However, it is probable that the nanostructure may have reduction in their integrity due to the oxidation of iodine if positive bias is applied for a very long time. The higher hydrogen
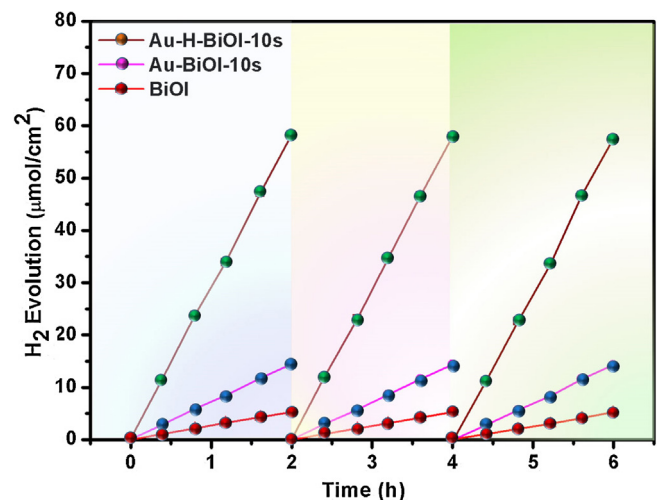

Fig. 6. Time courses of H$_2$ evolution for pristine BiOI, Au@BiOI, and Au@H-BiOI (250 °C) photoelectrodes under AM 1.5G solar simulator in 0.2 M Na$_2$SO$_4$ aqueous solution at an applied bias of 0.2 V vs RHE.

evolution in Au@BiOI (compared with BiOI) further confirms the contributions of Au NPs to the enhanced water splitting. The enhancements can arise from both the plasmonic effects and the catalytic effect of Au [57]. The highest hydrogen evolution in the Au@H-BiOI electrodes indicates that the synergy of Au NPs and hydrogenation further improves the performance in the PEC hydrogen evolution.

4. Conclusion

In summary, composites consisting of Au NPs and hydrogenated p-type BiOI NFAs have been developed as hydrogen-evolving photocathodes for PEC devices. The composite electrodes provide platforms for the study of the defect engineering in semiconductors and the plasmon-enhanced photoelectrochemistry. The enhanced performances of the Au@H-BiOI photocathodes with regard to photocurrent, Faradaic efficiency, and photoconversion efficiency can be attributed to the plasmonic effects of Au NPs, the

hydrogenation-induced oxygen vacancies, and the small thickness of NFAs. Future work on separating and controlling the various plasmonic effects will be of significance for both the fundamental understanding of electron and energy transfer in the composite photoelectrodes and the optimal operation of the PEC cells.

Competing financial interests

Acknowledgments

Appendix A. Supplementary data

Supplementary data associated with this article can be found, in the online version, at http://dx.doi.org/10.1016/j.electacta.2016.09.148.

References

[1] C.X. Kronawitter, J.R. Bakke, D.A. Wheeler, W.C. Wang, C.L. Chang, B.R. Antoun, J.Z. Zhang, J.H. Guo, S.F. Bent, S.S. Mao, L. Vayssieres, Electron Enrichment in 3d Transition Metal Oxide Hetero-Nanostructures, Nano Lett. 11 (2011) 3855–3861.

[2] T.F. Jiang, T.F. Xie, W.S. Yang, L.P. Chen, H.M. Fan, D.J. Wang, Photoelectrochemical and Photovoltaic Properties of p-n Cu2O Homojunction Films and Their Photocatalytic Performance, J. Phys. Chem. C 117 (2013) 4619–4624.

[3] A. Fujishima, K. Honda, Electrochemical Photolysis of Water at a Semiconductor Electrode, Nature 238 (1972) 37–38.

[4] J.Y. Gan, X.H. Lu, Y.X. Tong, Towards highly efficient photoanodes: boosting sunlight-driven semiconductor nanomaterials for water oxidation, Nanoscale 6 (2014) 7142–7164.

[5] R. Abe, Recent progress on photocatalytic and photoelectrochemical water splitting under visible light irradiation, J. Photochem. Photobio. C—Photochem. Rev. 11 (2010) 179–209.

[6] S. Choudhary, S. Upadhyay, P. Kumar, N. Singh, V.R. Satsangi, R. Shrivastav, S. Dass, Nanostructured bilayered thin films in photoelectrochemical water splitting—A review, Int. J. Hydrogen Energy 37 (2012) 18713–18730.

[7] D. Eisenberg, H.S. Ahn, A.J. Bard, Enhanced Photoelectrochemical Water Oxidation on Bismuth Vanadate by Electrodeposition of Amorphous Titanium Dioxide, J. Am. Chem. Soc. 136 (2014) 14011–14014.

[8] Y.C. Qiu, K.Y. Yan, H. Deng, S.H. Yang, Secondary Branching and Nitrogen Doping of ZnO Nanotetrapods: Building a Highly Active Network for Photoelectrochemical Water Splitting, Nano Lett. 12 (2012) 407–413.

[9] H.K. Wang, A.L. Rogach, Hierarchical SnO2 Nanostructures: Recent Advances in Design, Synthesis, and Applications, Chem. Mater. 26 (2014) 123–133.

[10] K.C. Leonard, K.M. Nam, H.C. Lee, S.H. Kang, H.S. Park, A.J. Bard, ZnWO4/WO3 Composite for Improving Photoelectrochemical Water Oxidation, J. Phys. Chem. C 117 (2013) 15901–15910.

[11] Q.C. Liu, D.K. Ma, Y.Y. Hu, Y.W. Zeng, S.M. Huang, Various Bismuth Oxyiodide Hierarchical Architectures: Alcohothermal-Controlled Synthesis, Photocatalytic Activities, and Adsorption Capabilities for Phosphate in Water, ACS Appl, Mater. Interfaces 5 (2013) 11927–11934.

[12] J. Cao, B.Y. Xu, H.L. Lin, B.D. Luo, S.F. Chen, Novel heterostructured Bi2S3/BiOI photocatalyst: facile preparation, characterization and visible light photocatalytic performance, Dalton Trans. 41 (2012) 11482–11490.

[13] C.X. Liao, Z.J. Ma, G.P. Dong, J.R. Qiu, BiOI nanosheets decorated TiO2 nanofiber: Tailoring water purification performance of photocatalyst in structural and photo-responsivity aspects, Appl. Surf. Sci. 314 (2014) 481–489.

[14] J. Yang, L.J. Xu, C.L. Liu, T.P. Xie, Preparation and photocatalytic activity of porous Bi5O7I nanosheets, Appl. Surf. Sci. 319 (2014) 265–271.

[15] Y.C. Huang, H.B. Li, M.S. Balogun, W.Y. Liu, Y.X. Tong, X.H. Lu, H.B. Ji, Oxygen Vacancy Induced Bismuth Oxyiodide with Remarkably Increased Visible-Light Absorption and Superior Photocatalytic Performance, ACS Appl. Mater. Interfaces 6 (2014) 22920–22927.

[16] A.C. Mera, Y. Moreno, J.Y. Pivan, O. Pena, H.D. Mansilla, Solvothermal synthesis of BiOI microspheres: Effect of the reaction time on the morphology and photocatalytic activity, J. Photochem. Photobio. A- Chem. 289 (2014) 7–13.

[17] N.T. Hahn, S. Hoang, J.L. Self, C.B. Mullins, Spray Pyrolysis Deposition and Photoelectrochemical Properties of n-Type BiOI Nanoplatelet Thin Films, ACS Nano 6 (2012) 7712–7722.

[18] E. Ozbay, Plasmonics: Merging photonics and electronics at nanoscale dimensions, Science 311 (2006) 189–193.

[19] M.A. Green, S. Pillai, Harnessing plasmonics for solar cells, Nat. Photon. 6 (2012) 130–132.

[20] A.G. Brolo, Plasmonics for future biosensors, Nat. Photon. 6 (2012) 709–713.

[21] Y.B. Zheng, L. Jensen, W. Yan, T.R. Walker, B.K. Juluri, L. Jensen, T.J. Huang, Chemically Tuning the Localized Surface Plasmon Resonances of Gold Nanostructure Arrays, J. Phys. Chem. C 113 (2009) 7019–7024.

[22] B.B. Rajeeva, D.S. Hernandez, M.S. Wang, E. Perillo, L.H. Lin, L. Scarabelli, B. Pingali, L.M. Liz-Marzan, A.K. Dunn, J.B. Shear, Y.B. Zheng, Regioselective Localization and Tracking of Biomolecules on Single Gold Nanoparticles, Adv. Sci. 2 (2015).

[23] J. Renger, R. Quidant, N. van Hulst, L. Novotny, Surface-Enhanced Nonlinear Four-Wave Mixing, Phys. Rev. Lett 104 (2010) 046803.

[24] Y.B. Zheng, J.L. Payton, T.B. Song, B.K. Pathem, Y.X. Zhao, H. Ma, Y. Yang, L. Jensen, A.K.Y. Jen, P.S. Weiss, Surface-Enhanced Raman Spectroscopy To Probe Photoreaction Pathways and Kinetics of Isolated Reactants on Surfaces: Flat versus Curved Substrates, Nano Lett. 12 (2012) 5362–5368.

[25] R. Kumar, H. Zhou, S.B. Cronin, Surface-enhanced Raman spectroscopy and correlated scanning electron microscopy of individual carbon nanotubes, Appl. Phys. Lett 91 (2007) 223105.

[26] S.A. Maier, P.G. Kik, H.A. Atwater, S. Meltzer, E. Harel, B.E. Koel, A.A.G. Requicha, Local detection of electromagnetic energy transport below the diffraction limit in metal nanoparticle plasmon waveguides, Nat. Mater. 2 (2003) 229–232.

[27] M. Hu, J.Y. Chen, Z.Y. Li, L. Au, G.V. Hartland, X.D. Li, M. Marquez, Y.N. Xia, Gold nanostructures: engineering their plasmonic properties for biomedical applications, Chem. Soc. Rev. 35 (2006) 1084–1094.

[28] T. Kaelberer, V.A. Fedotov, N. Papasimakis, D.P. Tsai, N.I. Zheludev, Toroidal Dipolar Response in a Metamaterial, Science 330 (2010) 1510–1512.

[29] M.Y. Sha, H. Xu, S.G. Penn, R. Cromer, SERS nanoparticles: a new optical detection modality for cancer diagnosis, Nanomedicine (Lond) 2 (2007) 725–734.

[30] B.B. Rajeeva, R. Menz, Y.B. Zheng, Towards rational design of multifunctional theranostic nanoparticles: what barriers do we need to overcome? Nanomedicine (Lond) 9 (2014) 1767–1770.

[31] W.B. Hou, S.B. Cronin, A Review of Surface Plasmon Resonance-Enhanced Photocatalysis, Adv. Funct. Mater. 23 (2013) 1612–1619.

[32] M. Rycenga, C.M. Cobley, J. Zeng, W.Y. Li, C.H. Moran, Q. Zhang, D. Qin, Y.N. Xia, Controlling the Synthesis and Assembly of Silver Nanostructures for Plasmonic Applications, Chem. Rev. 111 (2011) 3669–3712.

[33] A. Primo, T. Marino, A. Corma, R. Molinari, H. Garcia, Efficient Visible-Light Photocatalytic Water Splitting by Minute Amounts of Gold Supported on Nanoparticulate CeO2 Obtained by a Biopolymer Templating Method, J. Am. Chem. Soc. 133 (2011) 6930–6933.

[34] Z.W. Liu, W.B. Hou, P. Pavaskar, M. Aykol, S.B. Cronin, Plasmon Resonant Enhancement of Photocatalytic Water Splitting Under Visible Illumination, Nano Lett. 11 (2011) 1111–1116.

[35] C. Burda, X.B. Chen, R. Narayanan, M.A. El-Sayed, Chemistry and properties of nanocrystals of different shapes, Chem. Rev. 105 (2005) 1025–1102.

[36] G.M. Wang, Y.X. Ling, X.H. Lu, F. Qian, Y.X. Tong, J.Z. Zhang, V. Lordi, C.R. Leao, Y. Li, Computational and Photoelectrochemical Study of Hydrogenated Bismuth Vanadate, J. Phys. Chem. C 117 (2013) 10957–10964.

[37] G.M. Wang, H.Y. Wang, Y.C. Ling, Y.C. Tang, X.Y. Yang, R.C. Fitzmorris, C.C. Wang, J.Z. Zhang, Y. Li, Hydrogen-Treated TiO2 Nanowire Arrays for Photoelectrochemical Water Splitting, Nano Lett. 11 (2011) 3026–3033.

[38] H.Y. Wang, G.M. Wang, Y.C. Ling, M. Lepert, C.C. Wang, J.Z. Zhang, Y. Li, Photoelectrochemical study of oxygen deficient TiO2 nanowire arrays with CdS quantum dot sensitization, Nanoscale 4 (2012) 1463–1466.

[39] P. Kwolek, K. Szacilowski, Photoelectrochemistry of n-type bismuth oxyiodide, Electrochim. Acta 104 (2013) 448–453.

[40] J.Y. Gan, X.H. Lu, B.B. Rajeeva, R. Menz, Y.X. Tong, Y.B. Zheng, Efficient Photoelectrochemical Water Oxidation over Hydrogen-Reduced Nanoporous BiVO4 with Ni-B-i Electrocatalyst, ChemElectroChem 2 (2015) 1385–1395.

[41] S.Y. Chae, H. Jung, H.S. Jeon, B.K. Min, Y.J. Hwang, O.S. Joo, Morphology control of one-dimensional heterojunctions for highly efficient photoanodes used for solar water splitting, J. Mater. Chem. A 2 (2014) 11408–11416.

[42] T.W. Kim, K.S. Choi, Nanoporous BiVO4 Photoanodes with Dual-Layer Oxygen Evolution Catalysts for Solar Water Splitting, Science 343 (2014) 990–994.

[43] J. Zhao, A.O. Pinchuk, J.M. Mcmahon, S.Z. Li, L.K. Ausman, A.L. Atkinson, G.C. Schatz, Methods for Describing the Electromagnetic Properties of Silver and Gold Nanoparticles, Acc. Chem. Res. 41 (2008) 1710–1720.

[44] S.S. Yao, K.N. Ding, Y.F. Zhang, The effects of the introduction of Al atom into monoclinic BiVO4: a theoretical prediction, Theor. Chem. Acc. 127 (2010) 751–757.

[45] J.Y. Gan, X.H. Lu, J.H. Wu, S.L. Xie, T. Zhai, M.H. Yu, Z.S. Zhang, Y.C. Mao, S.C.I. Wang, Y. Shen, Y.X. Tong, Oxygen vacancies promoting photoelectrochemical performance of In2O3 nanocubes, Sci. Rep 3 (2013) 1021.

[46] Y.J. Lin, S. Zhou, X.H. Liu, S. Sheehan, D.W. Wang, TiO2/TiSi2 Heterostructures for High-Efficiency Photoelectrochemical H2O Splitting, J. Am. Chem. Soc. 131 (2009) 2772–2773.

[47] H.M. Chen, C.K. Chen, C.J. Chen, L.C. Cheng, P.C. Wu, B.H. Cheng, Y.Z. Ho, M.L. Tseng, Y.Y. Hsu, T.S. Chan, J.F. Lee, R.S. Liu, D.P. Tsai, Plasmon Inducing Effects for

Enhanced Photoelectrochemical Water Splitting: X-ray Absorption Approach to Electronic Structures, ACS Nano 6 (2012) 7362–7372.

[48] J.R. McKone, A.P. Pieterick, H.B. Gray, N.S. Lewis, Hydrogen Evolution from Pt/Ru-Coated p-Type WSe2 Photocathodes, J. Am. Chem. Soc. 135 (2013) 223–231.

[49] V. Spagnol, E. Sutter, C. Debiemme-Chouvy, H. Cachet, B. Baroux, EIS study of photo-induced modifications of nano-columnar TiO2 films, Electrochim. Acta 54 (2009) 1228–1232.

[50] S.F. Karmanenko, A.I. Dedyk, N.N. Isakov, A.S. Gordeichuk, A.A. Semenov, L.T. Ter-Martirosyan, J. Hagberg, Study of the effect of manganese impurities on dielectric characteristics of BSTO films, Tech. Phys. 46 (2001) 498–502.

[51] C.H. Park, S.B. Zhang, S.H. Wei, Origin of p-type doping difficulty in ZnO: The impurity perspective, Phys. Rev. B 66 (2002) 073202.

[52] T. Jungwirth, J. Sinova, A. MacDonald, B. Gallagher, V. Novák, K. Edmonds, A. Rushforth, R. Campion, C. Foxon, L. Eaves, Character of states near the Fermi level in (Ga Mn) As: Impurity to valence band crossover, Phys. Rev. B 76 (2007) 125206.

[53] D.C. Cronemeyer, Infrared Absorption of Reduced Rutile Tio2 Single Crystals, Phys. Rev. 113 (1959) 1222–1226.

[54] S.C. Warren, E. Thimsen, Plasmonic solar water splitting, Energy Environ. Sci. 5 (2012) 5133–5146.

[55] S.A. Maier, Localized Surface Plasmons, Plasmonics: Fundamentals and Applications, Springer, New York, 2006.

[56] K.F. Wu, Z.Y. Chen, H.J. Lv, H.M. Zhu, C.L. Hill, T.Q. Lian, Hole Removal Rate Limits Photodriven H-2 Generation Efficiency in CdS-Pt and CdSe/CdS-Pt Semiconductor Nanorod-Metal Tip Heterostructures, J. Am. Chem. Soc. 136 (2014) 7708–7716.

[57] J.A. Christians, R.C.M. Fung, P.V. Kamat, An Inorganic Hole Conductor for Organo-Lead Halide Perovskite Solar Cells. Improved Hole Conductivity with Copper Iodide, J. Am. Chem. Soc. 136 (2014) 758–764.

[58] Y. Tian, T. Tatsuma, Mechanisms and applications of plasmon-induced charge separation at TiO2 films loaded with gold nanoparticles, J. Am. Chem. Soc. 127 (2005) 7632–7637.

[59] J. Lee, S. Mubeen, X.L. Ji, G.D. Stucky, M. Moskovits, Plasmonic Photoanodes for Solar Water Splitting with Visible Light, Nano Lett. 12 (2012) 5014–5019.